# Structural Investigation of Uranium−Neptunium Mixed Oxides Using XRD, XANES, and ^{17}O MAS NMR

Laura Martel,*,[†] Jean-Francois Vigier,[†] Damien Prieur,[†] Sarah Nourry,[†] Antony Guiot,[†] Kathy Dardenne,[‡] Jacobus Boshoven,[†] and Joseph Somers[†]

[†]European Commission, Joint Research Centre, Institute for Transuranium Elements, Hermann von Helmholtz Platz 1 76344 Eggenstein Leopoldshafen, Germany

[‡]Karlsruhe Institute of Technology, Institut für Nukleare Entsorgung (INE), Hermann von Helmholtz Platz 1, 76344 Eggenstein Leopoldshafen, Germany

ABSTRACT: Uranium−neptunium mixed dioxides are con sidered as fuels and targets for the transmutation of the minor actinides in fast neutron reactors. Hereafter, a local and atomic scale structural analysis was performed on a series of $U_{1-x}Np_xO_2$ (x = 0.01; 0.05; 0.20; 0.50; 0.75; 0.85) synthesized by the sol−gel external gelation method, for which longer range structural analysis indicates that the process yields solid solutions. The oxidation state of IV for uranium and neptunium cations was confirmed using U L_{III} and Np L_{III} edge X ray absorption near edge structure (XANES). The atomic scale structure was probed with ^{17}O magic angle spinning nuclear magnetic resonance (MAS NMR) for the anion. Structural distortions due to the substitution of U by the smaller Np cation were detected by ^{17}O MAS NMR.
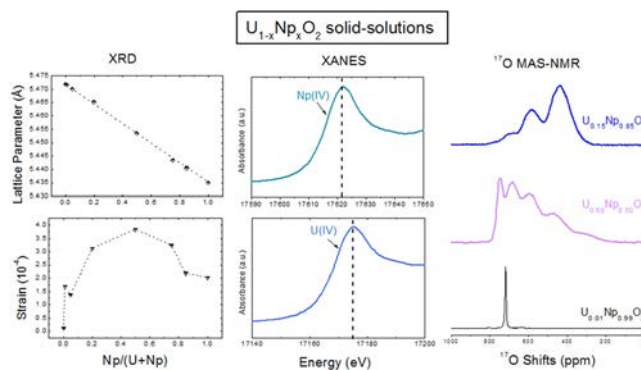
1. INTRODUCTION

Understanding the incorporation mechanism of minor actinides (MA), that is, Np, Am, Cm, in uranium dioxides and mixed U− Pu oxides (MOX) as solid solutions is essential starting point for the detailed understanding of these materials, which will become particularly relevant, as they are considered as fuels and targets for the transmutation of the minor actinides in fast neutron reactors.[1,2] This is an innovative approach to dramatically reduce the long term radiotoxic impact of these materials and is considered in two modes: the homogeneous MA recycling scenario which relies on the introduction of a few percent of MA in all of the fuel pins of the reactor and, the heterogeneous MA recycling concept which considers deploy ment of the MA in a UO_2 matrix in dedicated fuel rods and assemblies. As such fuels contain no Pu in the fresh fuel, they are often referred as "targets". Despite being the most abundant minor actinide in spent fuel, targets bearing Np have not been, to our knowledge, the subject of any complete structural study using local structure techniques. We focus our attention here on a most basic solid solution system $U_{1-x}Np_xO_2$. Such Np solid solutions have been investigated by XRD at high temperatures to develop the understanding of their thermody namic properties in the hyperstoichiometric region of the system.[3−5] Further, as these materials possess unusual magnetic ordering at low temperatures significant investigative work have been done.[6−9] Neptunium 237 Mössbauer spectroscopy was performed in a series of $U_{1−x}Np_xO_2$ (x = 0.15, 0.25, 0.5, 0.75,

1) compounds and demonstrated that Np remains IV valent oxidation state for all compositions.[7] Nevertheless, the oxidation state of uranium in these compounds remains uncharacterized, despite its potential importance as U can adopt higher oxidation states than IV, that is, V and VI.

Structural analysis of actinide solid solutions such as $Th_{1−x}M_xO_2$ (M = U, Pu)[10] and $U_{1−x}Pu_xO_2$[11] were performed mainly using X ray absorption spectroscopy (XAS). Such studies show more complex local structures than derived from XRD characterization with, for example, a bimodal cation oxygen distribution. High resolution solid state MAS NMR should be a very efficient tool to probe the atomic scale in such compounds, as it has been extensively utilized for the study of, among other systems, rare earth solid solutions.[12−16] Never theless, until recently, its use with radioactive materials has remained elusive, mainly due to strict radiological safety requirements of handling highly radiotoxic materials when high spinning speeds are needed.[17] A technological advance has allayed these safety issues and our instrument at JRC ITU is now available for the characterization of such highly radioactive materials.[18] The combination of XAS and MAS NMR will be, then, very powerful for the study of these actinide solid solutions.

Herein, we present a complete analysis of the $U_{1-x}Np_xO_2$ (x = 0.01, 0.05, 0.2, 0.5, 0.75, 0.85, 1) solid solutions prepared by gel supported precipitation. The stoichiometry of the solid solution was checked by XRD. The oxidation state of both uranium and neptunium was determined using XANES. Finally, high resolution ^{17}O MAS NMR was used for the first time in such solid solutions to probe the local environment around the oxygen.

2. EXPERIMENTAL SECTION

2.1. Sample Preparation and Chemical Analysis. The $U_xNp_{1-x}O_2$ samples (x = 0.01, 0.05, 0.20, 0.50, 0.75, 0.85), denoted hereafter as Np_x, have been prepared by gel supported precipitation (also referred as sol−gel external gelation). This synthesis process avoids powder handling of the highly radiotoxic materials,[3,19] and one obtains a high composition (metal) homogeneity.[20] A uranyl nitrate solution was mixed with a nitric acid solution of ^{237}Np to achieve a molar stoichiometry of x = Np/(U + Np), as defined above. Before the external gel step, aliquots of each solution were taken for analysis by inductively coupled plasma − mass spectrometry (ICP MS) to perform a precise control of the Np/(U + Np) ratio. The results are presented in Table 1 and there is a good

Table 1. Chemical Analysis of the Six U_{1-x} Np_xO_2 Compounds

compound name	Np (mol %)	U (mol %)
Np1	1.0(6)	99.0(6)
Np5	4.7(6)	95.3(6)
Np20	19.1(3)	80.9(3)
Np50	51.18(4)	48.81(4)
Np75	75.8(4)	24.2(1)
Np85	85.9(5)	14.10(7)

agreement between calculated and obtained compositions. For the external gelation step, an organic thickener (Methocel, Dow Chemicals) was added to increase the viscosity of the solutions. These were then dropped into an ammonia bath where the droplet to particle conversion took place due to hydroxide precipitation of the metals inside the polymer backbone of the droplet. The resulting beads were washed, dried, and then calcined at 600 °C in air (2 h) to remove organics and then at 700 °C in Ar/H_2 (2 h) to ensure the reduction to U(IV). The samples were enriched at about 30% in ^{17}O by heating in oxygen 17 enriched gas at 800 °C during 24 h, before being sintered at 1650 °C (4 h) under Ar/H_2.

2.2. X-ray Diffraction. The XRD patterns were obtained at room temperature on 20 mg of a powdered sample loaded in an epoxy resin to fix the powders and avoid their dispersion. A Bruker D8 Advance diffractometer (Cu Kα radiation, 40 kV, and 40 mA) with a Bragg−Brentano $\theta/2\theta$ configuration and implanted in a radioactive glovebox were used for the analysis. This diffractometer is equipped with a curved Ge mono chromator (111) and a Lynxeye linear position sensitive. Instrumental calibration was done using LaB_6 SRM660a as external standard. The powder patterns were recorded using a step size of 0.0197° across the angular range $10° \leq 2\theta \leq 120°$. Structural analyses were performed by the Rietveld method using Jana2006 software.[21] Peak profile fitting was achieved using Pseudo Voigt functions.

2.3. XANES. The XANES measurements were performed on 5 mg of powdered sample mixed with 55 mg of BN. The data were collected at the Angströmquelle Karlsruhe (ANKA) synchrotron, under dedicated operating conditions (2.5 GeV, 100−160 mA) at the INE Beamline for actinide science, on which XAS on radioactive materials is licensed.[22] A Ge [422] double crystal monochromator coupled to collimating and focusing Rh coated mirrors was used. The spectra were acquired at room temperature in both transmission and fluorescence modes at U L_{III} (17166 eV) and Np L_{III} (17610 eV) edges. In this latter mode, XAS were recorded using a five element LEGe solid state detector. The energy calibration was accomplished by measuring the spectrum of an Y (17038 eV) foil located between the second and the third ion chamber filled with Ar at ambient pressure, used to record the transmission.

2.4. ^{17}O MAS NMR. The NMR experiments were performed on a 9.4 T Bruker spectrometer at the Larmor
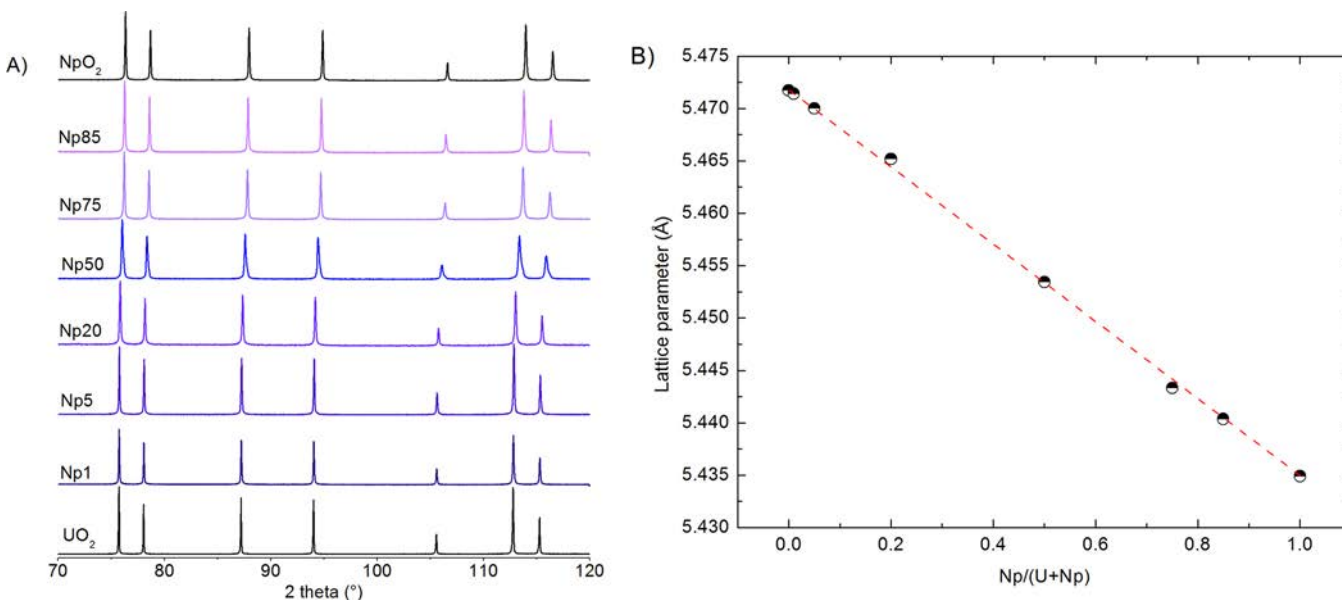

Figure 1. (A) XRD pattern of the $U_{1-x}Np_xO_2$ solid solutions and (B) variation of the lattice parameter as a function of composition.

frequency of 54.25 MHz. This equipment is combined with an active glovebox dedicated to the handling of radioactive materials, and is described in detail elsewhere.[23] A commercial 1.3 mm probe was used, and the rotors were spun at 55 kHz. The pulse durations were 4 μs ($\pi/2$) and 8 μs (π), respectively, with an echo delay of 18.2 μs (1 rotor period). All spectra were calibrated relative to H_2O enriched in ^{17}O (0 ppm). The longitudinal relaxation time (T_1) was determined using an inversion−recovery pulse sequence. All the spectra were fitted using the dmfit software and the option "quad first".[24]

3. RESULTS AND DISCUSSION

3.1. Synthesis and Long-Range Structure. The XRD patterns of the well crystallized $U_{1-x}Np_xO_2$ samples are presented in Figure 1A. These data indicate that all the samples are single phase solid solutions, except for the Np50, for which evidence for two fluorite crystalline phases is found. The presence of two phases in this later sample is most probably due to the experimental conditions during the synthesis and not to a miscibility gap, as this material has already been synthesized as a single phase.[9] Using the Rietveld refinement method, the lattice parameters of each sample were precisely determined, and their variation as a function of composition is presented in Figure 1B. The fluorite $Fm3m$ crystalline structure was found for all the materials. The two crystalline phases identified in Np50 were determined as $U_{0.50}Np_{0.50}O_2$ (86%) and $U_{0.25}Np_{0.75}O_2$ (14%) based on their lattice parameter. As this second phase impurity is very small and given the radiological hazard and our active adherence to the radiological protection of the staff (ALARA − as low as reasonably achievable), the synthesis was not repeated. All the lattice parameters do follow the Vegard's law exceptionally well, indicating good mixing in the solid solutions. In addition, the diffraction peak broadening was analyzed using Hall− Williamson formula to extract the micro strain in these materials.[25] For the Np50 sample, only the strain of the $U_{0.5}Np_{0.5}O_2$ component has been considered. The results are shown in Figure 2 and indicate a higher strain for the intermediate solid solutions. This trend is readily understood in terms of local distortion created by the coexistence of two cations with different ionic radius in the structure as shown, for example, by Venkateswara Rao et al. in $Mg_{1-x}Ni_xO$[26] or by Düvel et al. in mixed alkaline earth fluorine.[27]
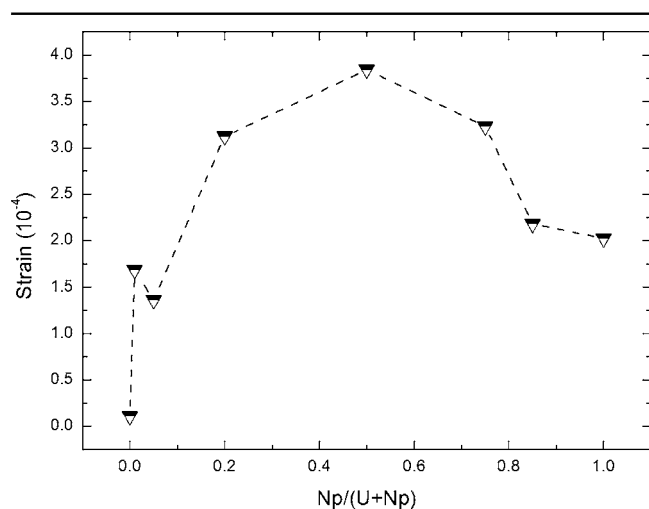
Figure 2. Strain variation for the different $U_{1-x}Np_xO_2$ samples.

3.2. Oxidation States Determination of the Actinides. The oxidation states have been determined from XANES at U L_{III} and Np L_{III} edges. The corresponding spectra are presented in Figure 3 with those of $U(IV)O_2$ and $Np(IV)O_2$ reference
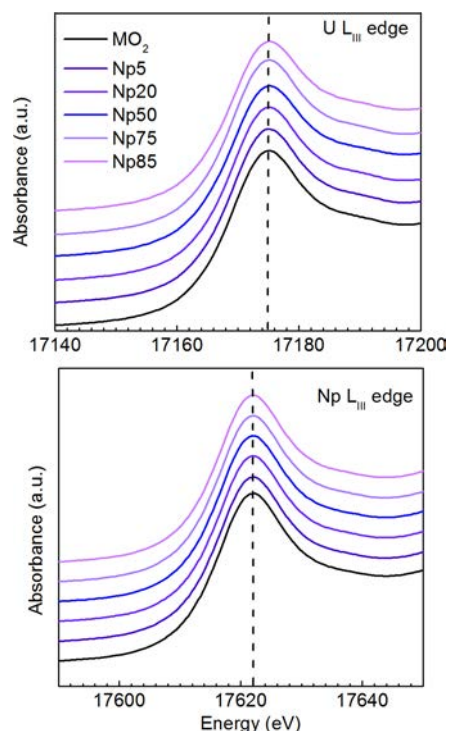
Figure 3. XANES spectra at the U L_{III} and Np L_{III} edges of MO_2 (M = U or Np) and of the $U_{1-x}Np_xO_2$ samples.

materials. Their inflection points and white lines were found at 17170.3 (5) and 17175.5 (5) eV and at 17616.5 (5) and 17621.8 (5) eV, respectively. Within the uncertainty of 0.5 eV, there is no variation of the inflection point and the white lines in the $U_{1-x}Np_xO_2$ samples compared to the pure dioxides (Table S1). This shows that uranium and neptunium have an oxidation state of IV for all the compositions. The oxidation state IV of Np in the $U_{1-x}Np_xO_2$ is consistent with previous Mössbauer results.[7] Due to the very close UL_{III} and NpL_{III} edges, EXAFS spectra cannot be analyzed with this conven tional XAS.

3.3. Local Structure Determination by ^{17}O MAS NMR. The ^{17}O MAS NMR experiments were performed to probe the local environment around the anions. Due to the presence of unpaired electrons in the cation's $5f$ shell, the NMR resonance of the anion is shifted beyond the normal range found for traditional chemical shifts. This so called paramagnetic shift is very sensitive to the oxidation states, orbital occupancy, and coordinating geometries of the neighboring cations. In addition, a variation in chemical composition due to the substitution of a cation by another one leads to the apparition of additional peaks on the MAS NMR spectra corresponding to the different local environments around the anion.[27−30] This specificity of paramagnetic NMR is therefore very efficient for character ization of such solid solutions. The full spectra, the center band, and the corresponding fits are presented in Figure 4 for UO_2, NpO_2, and the $U_{1-x}Np_xO_2$ under study. Spinning sidebands have been identified for all the spectra and are coming from the satellite transitions. The signals of the two end members,
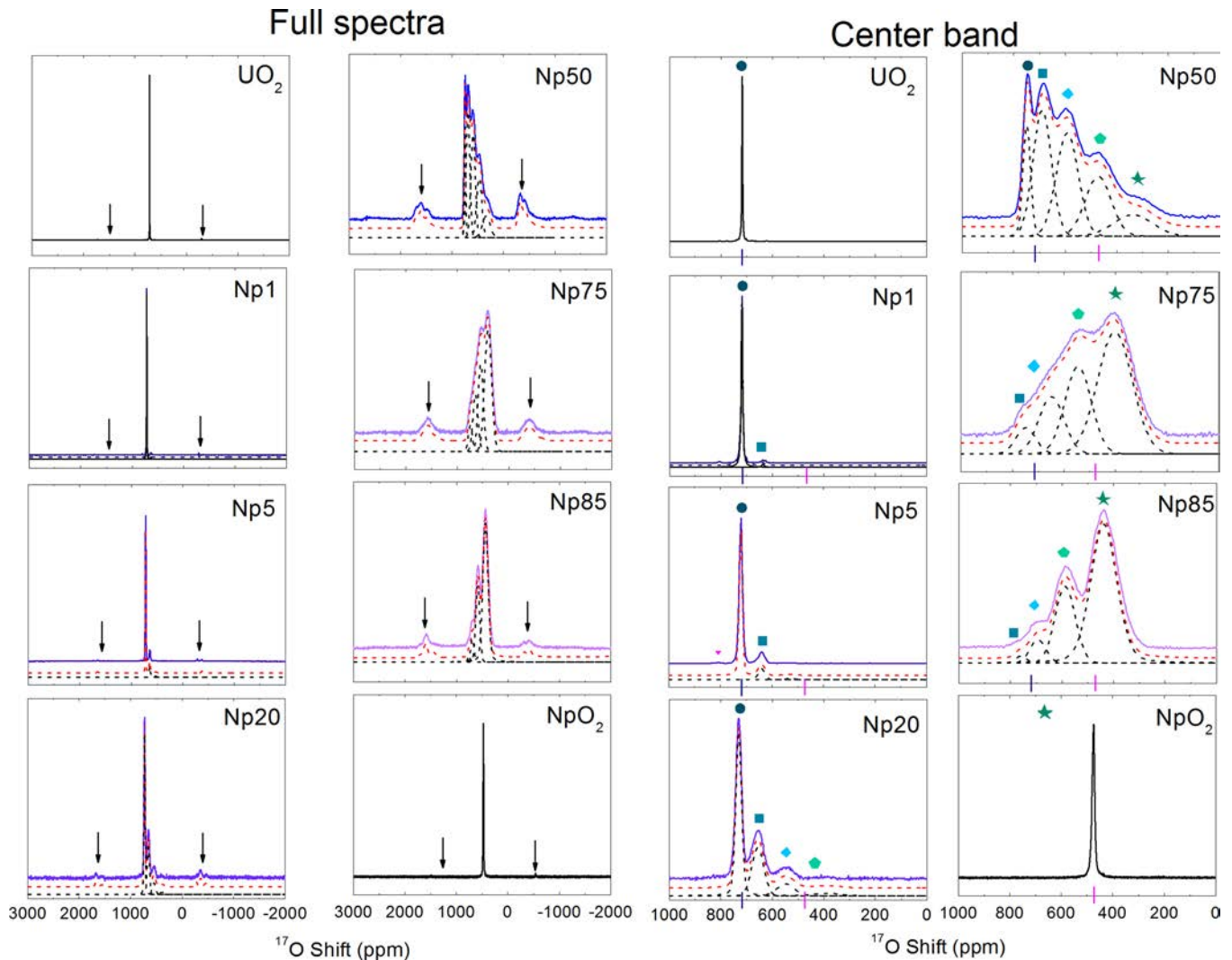
Figure 4. ^{17}O MAS NMR spectra and fits (red and black curves) of the $U_{1-x}Np_xO_2$ samples acquired at 55 kHz. The black arrows indicate the spinning sidebands positions.

identified at 717 and 475 ppm for UO_2 and NpO_2 respectively,[18] exhibit a single sharp peak characteristic of $O(U)_4$ and $O(Np)_4$ units within the sample. The different oxygen signals observed by increasing Np content are attributed to $O(Np)_y(U)_{4-y}$ (with $0 \leq y \leq 4$) units. The ^{17}O MAS spectrum of Np1, characteristic of the lowest Np concentration in our series, is composed of two signals at 718.4 and 636.3 ppm, attributed to $(O(U)_4)$ and $(O(U)_3(Np)_1)$ units. In contrast with XRD where the change of lattice parameter compared to UO_2 is too small to prove clearly the formation of a solid solution, ^{17}O MAS spectrum of Np1 gives, here, a clear indication of solid solution formation for such low Np amounts. With an increase of 4 mol % of NpO_2 (Np5 sample), three signals are now visible at 720.9 $(O(U)_4)$, 639.9 $(O(U)_3(Np)_1)$, and 527 ppm $(O(U)_2(Np)_2)$. The NMR spectrum of the Np20 sample is composed of four signals between 729.7 ppm $(O(U)_4)$ and 414.3 ppm $(O(U)_1(Np)_3)$. For the Np50 compound, the two crystalline phases observed by XRD cannot be differentiated on the MAS NMR spectrum due to the width of the peaks identified between 749.9 ppm $(O(U)_4)$ and 337.0 ppm $(O(Np)_4)$ and a strong overlapping of the two spectra. Nevertheless, as the $U_{0.50}Np_{0.50}O_2$ is the dominant composition, the position of the peaks should be characteristic of a sample with this composition. The Np75 sample has an NMR spectrum, which is the least well resolved of all, but, four signals can still be differentiated between 759.8 ppm $(O(U)_3(Np)_1)$ and 405.2 ppm $(O(Np)_4)$. Finally, the spectrum of the Np85 sample presents four well resolved signals between 759.6 ppm $(O(U)_3(Np)_1)$ and 437.8 ppm $(O(Np)_4)$.

The variation of the paramagnetic shifts of the five different subunits with sample composition is presented in Figure 5. For each identical $O(Np)_y(U)_{4-y}$ (with $(0 \leq y \leq 4)$) unit, there is a uniform linear increase of the shifts with increasing $Np/(U + Np)$ content. It is also worth noticing that the slope of the linear fit of the paramagnetic shifts increases with increasing number of Np neighbors. This linear increase of the shifts with increasing $Np/(U + Np)$ content is in agreement with the existence of a solid solution through the entire composition as observed by XRD. In fact, similar variations of the shifts were observed by NMR in alkaline earth[27,31,32] and rare earth solid solutions.[15] The variation of the shift of each unit with total composition can be thus deemed as an NMR analogue to the Vegard Law's. The variation of the shifts is more pronounced in our series of solid solution due to the paramagnetic effect, which can be very sensitive to any local distortions.[13,14] Presence of local distortions were observed on similar,
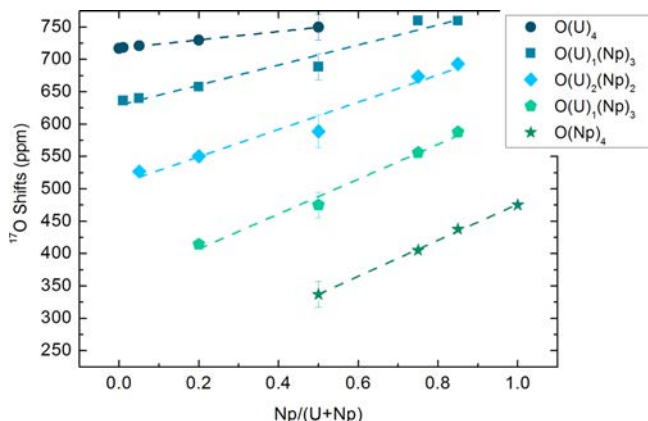
Figure 5. Variation of the ^{17}O paramagnetic shifts with composition for the different $O(Np)_y(U)_{1-y}$ (with $(0 \leq y \leq 4)$) units. The dashed lines represent the linear fits.

$Th_{1-x}U_xO_2$ and $Th_{1-x}Pu_xO_2$, solid solutions from previous EXAFS measurements done by Hubert et al.[10] (Th is the cation with the higher ionic radius). The authors observed a larger Th−O bond distance than the weighted cation−anion bond distance determined based on the lattice parameter and, in contrast, a shorter U−O or Pu−O bond length. As our system is quite similar to these materials, with Np insertion (smaller ionic radii), higher U−O bond and smaller Np−O bond compared to the average bond distances should be expected. It is difficult to delve further in the analysis of the origin of the paramagnetic shifts and determine if this interaction occurs through bond (Fermi contact) or through space (pseudocontact) as it is systematically performed for other paramagnetic systems, mainly due to the lack of experimental structural data in these types of materials and the difficulties to perform theoretical calculations of the shifts on such complicated $5f$ systems.

The width of the individual peak characterized by its full width at half maximum (fwhm), has been plotted against the Np/(U + Np) ratio in Figure 6. For the same composition, the presence of at least one neptunium neighbor around the O atom leads to an increase of the fwhm and the more surrounding Np atoms the larger the fwhm. In addition, the
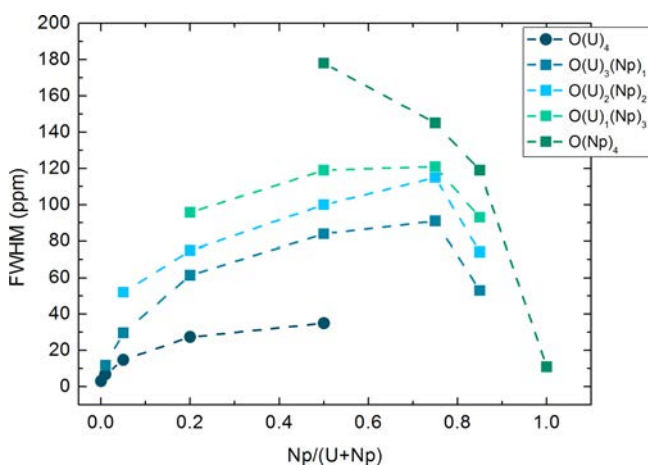

Figure 6. Variation of the fwhm of the five different $O(Np)_y(U)_{4-y}$ (with $(0 \leq y \leq 4)$) units with composition. The dashed lines are a guide for the eye.

increase of the fwhm with increasing Np neighbors is more important for the $O(Np)_4$ units than for the $O(U)_4$ units. For all the samples, there is an increase of this parameter for each coordination unit with increasing Np content until Np75, then it decreases. The variations of the fwhm can be attributed to both local distortions around the O atoms when Np^{4+} replaces U^{4+}[28] and transfer of positive electron from the cations.[27] Considering the variation of the strain obtained by XRD with a maximum for the $U_{0.5}Np_{0.5}O_2$, additional electronic effects must also contribute to the line broadening for which a maximum occurs for $U_{0.25}Np_{0.75}O_2$. It is worth mentioning that, as ^{17}O is a quadrupolar nucleus (i.e., spin 5/2), presence of local bond angle distortions around the oxygen atoms can create an appearance of quadrupole interaction[33] (i.e., a quadrupolar coupling constant (C_Q) not null) being at the origin of the fwhm increase previously observed. To verify if such a distortion exists, nutation experiments that consist of the observation of the center band magnetization variation with increasing 90° pulse lengths ($\tau_{90°}$) have been performed.[34−36] In fact, if one compares the nutation curve of a given compound with that of a reference sample, known with $C_Q = 0$ (usually a liquid sample), one can determine if $C_Q \neq 0$ (i.e., different variation of the nutation curves) and, if so, an estimate of its value is possible by fitting the nutation curve.[37,38] The nutation curves obtained at 55 kHz are presented in Figure S1 (2 W of applied power) and Figure S2 (20 W of applied power) for the samples that present the highest fwhm increase Np5, Np20, Np75, and Np85 (Np50 has not been analyzed as two crystalline phases are present). To obtain these nutation curves, the intensities of the main and best resolved peaks have been integrated. In addition, to compare the nutation curves of the different peaks, their intensities have been scaled at the same height. As MAS can influence the nutation curves by reducing the signal intensity at high pulse length,[39,40] the experiments were also performed at 40 kHz, but no differences were observed between these two spinning rates (not shown). All the nutation curves present similar variation with that of $H_2^{17}O$ ($C_Q = 0$), as well as between different $O(Np)_y(U)_{4-y}$ units for the same composition than through the composition range under study. A maximum intensity is detected around 4 μs at 20 W and 12.5 μs at 2 W. These results show that a perfect tetrahedral environment remains around the oxygen atoms even if An−O bond distortions are expected. The broadening observed for the different O unit with increasing Np atoms and content is therefore most probably due to anisotropic interactions created, among others, by the presence of delocalized $5f$ electrons and actinide−oxygen bond variations. Considering these results, all the spectra were acquired using the conditions $\tau_{90°}^{n.s.} = \tau_{90°}^{s}$ (with "n.s." the so called "nonselective" excitation expected in liquids and for cubic substances and "s" the so called "selective excitation" expected when $C_Q \neq 0$[34]).

The quantitative nature of NMR is one of the key attributes of this technique allowing site population determination for each different oxygen site. The quantitative spectra previously presented were obtained after determination of the 90° pulse excitation but also of the longitudinal relaxation times (T_1) for each O atom in the different environments in all of the samples. The T_1 variations for each different O unit and for all the chemical compositions are presented in Figure 7. For the five types of O subunits, T_1 decreases with the increasing Np content in the sample. This result shows that the addition of Np atom in the vicinity of the O atom leads to a decrease of T_1,
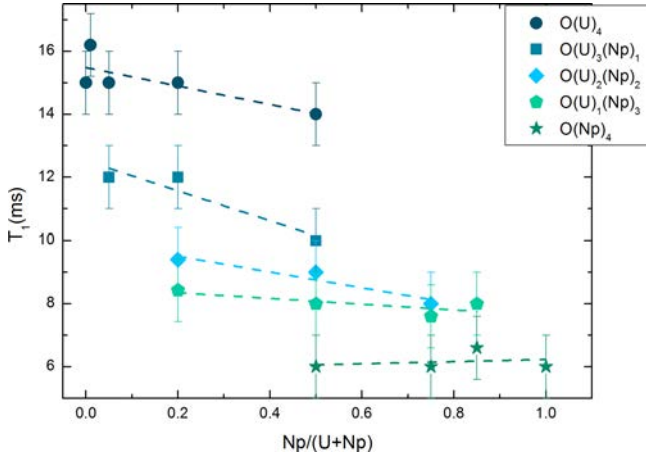
Figure 7. Variation of the longitudinal relaxation time (T_1) for the different $O(Np)_y(U)_{4-y}$ (with $(0 \leq y \leq 4)$) units with composition. The dashed lines are linear fits.

in perfect agreement with faster relaxation time for NpO_2 than UO_2.

In Figure 8, the integrated intensity of each $O(U)_y(Np)_{1-y}$ (with $(0 \leq y \leq 4)$) unit obtained experimentally were
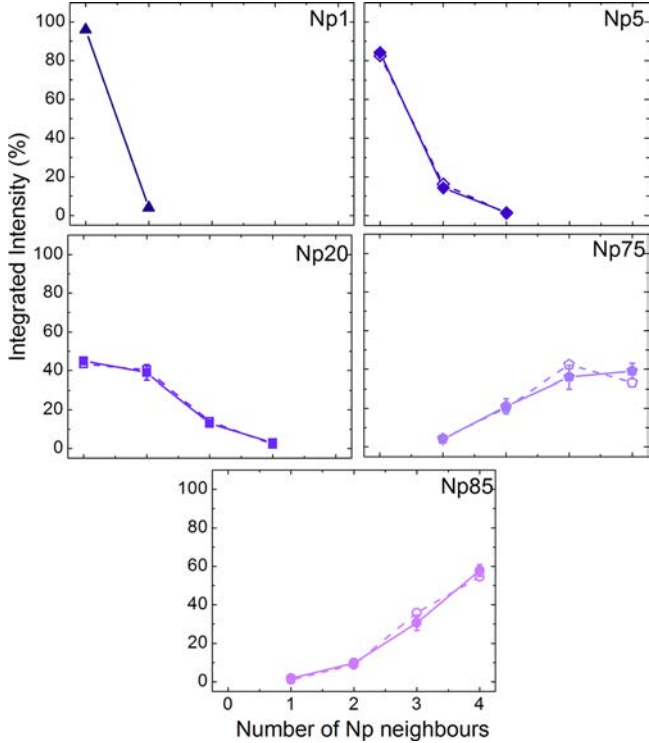

Figure 8. Plot of experimental (plain symbols and lines) and theoretical (dashed symbols and lines) intensities with the number of Np neighbors. The theoretical intensities correspond to a randomly distributed network. The uncertainties are included in the symbols.

compared to those expected for a randomly distributed network (RDN). The experimental integrated intensities were obtained by fitting the center band, but also the satellite transition intensities. The chemical shift anisotropy (CSA) values are given in Table 2. The values of the anisotropy of the CSA tensor increase when a cation with a different nature is added to the pure dioxide in agreement with the fwhm

evolution. The so called "$n = 0$" spinning sideband is expected to contribute to the signal intensity of the central transition as it lies below this one.[41] Due to the important spectral broadening, it has unfortunately not been possible to identify properly this later even by changing the spinning rate. The intensity of this spinning sideband has therefore been added in the error bars considering the intensity of the highest spinning sidebands. The theoretical values expected for a RDN were calculated using a binomial distribution function given by

$$P(nO) = \Omega \times p^n \times (1 - p)^{4-n} \qquad (1)$$

where Ω is the number of permutations, $p = x$ is the probability of finding a Np in $U_{1-x}Np_xO_2$, and n is the number of possible ways Np or U can be arranged around the O atom. As the Np50 sample is composed of two crystalline phases that cannot clearly be differentiated, this sample was excluded from the following analysis. A good agreement is found between theoretical and experimental relative intensities for each solid solution confirming the U/Np random distribution. This later observation do also confirm the previous attribution given to all the $O(U)_y(Np)_{1-y}$ (with $(0 \leq y \leq 4)$) units.

4. CONCLUSION

A complete analysis of the long range and atomic scale structure of $U_{1-x}Np_xO_2$ samples was performed for the first time using a combination of XRD, XANES, and high resolution solid state ^{17}O MAS NMR. The robustness of the external gelation synthesis was proven from XRD and Vegard law behavior. In addition, the presence of local distortions due to the coexistence of cations with different ionic radius was observed thanks to the micro strain. XANES has shown that U and Np remain tetravalent for all the compositions. Using ^{17}O MAS NMR, the different oxygen environments were detected thanks to their different paramagnetic shifts. A linear increase of the shifts with decreasing Np content was observed for each $O(Np)_y(U)_{1-y}$ (with $(0 \leq y \leq 4)$) unit consistent with the existence of a solid solution. For the same type of unit, the slope of this linear fit increases as the O is surrounded by increasing numbers of Np neighbors. Local distortions around the oxygen atom due to the substitution of U^{4+} by the smaller Np^{4+} and transfer of positive electron from the cation lead to a variation of the fwhm of the individual $O(Np)_y(U)_{1-y}$ components. Nutation experiments show that no bond angle distortions exist around the oxygen atoms with a perfect tetrahedral environment maintained. Longitudinal relaxation times studies show a decrease of T_1 with increasing Np content in agreement with a larger T_1 for UO_2 than for NpO_2. Finally, the comparison of the intensities in a randomly distributed network and those obtained based on the relative experimental area of the peaks shows a good agreement. The combination of all these techniques and, particularly, the use of solid state high resolution NMR open new routes for the fine characterization of radioactive materials. In addition, the NMR data should be a strong basis for development of future solid state NMR calculations, which are not yet possible for 5f electrons due to, among others, the lack of experimental results.

Caution! As these uranium−neptunium mixed oxides present considerable radiotoxicity hazards, they were all handled under carefully controlled dedicated laboratories at the Institute for Transuranium Elements in Karlsruhe. All steps were performed in hermetically sealed gloveboxes maintained at a relative negative pressure with respect to the laboratory.

Table 2. Values of Anisotropy of the Chemical Shift Anisotropy (CSA) Tensor (ΔCSA) and Asymmetry Parameters of the CSA Tensor (ηCSA) for the Six $U_{1-x}Np_xO_2$ Compounds

	$O(U)_y(Np)_{1-y}$ units	compound name					
		Np1	Np5	Np20	Np50	Np75	Np85
ΔCSA	$O(U)_4$	388.53	510	493	610		
	$O(U)_3(Np)_1$	1440.48	1484	1314	1441	1411.40	1451
	$O(U)_2(Np)_2$		1100	1497	1435	1492.82	1343
	$O(U)_1(Np)_3$				1169	999.42	1344
	$O(Np)_4$				1098	640.74	521
ηCSA	$O(U)_4$	0	0	0	0.1		
	$O(U)_3(Np)_1$	0	0.1	0	0.1	0.83	0.6
	$O(U)_2(Np)_2$		0.3	0.2	0.5	0.11	0.8
	$O(U)_1(Np)_3$				0.8	0.57	0.1
	$O(Np)_4$				0.4	0.88	0.6

AUTHOR INFORMATION

Corresponding Author

*E mail: laura.martel@ec.europa.eu.

Notes

The authors declare no competing financial interest.

REFERENCES

(1) Fernandez, A.; McGinley, J.; Somers, J.; Walter, M. Overview of past and current activities on fuels for fast reactors at the Institute for transuranium elements. *J. Nucl. Mater.* 2009, 392, 133−138. Lebreton, F.; Prieur, D.; Horlait, D.; Delahaye, T.; Jankowiak, A.; Léorier, C.; Jorion, F.; Gavilan, E.; Desmoulière, F. Recent progress on minor actinide bearing oxide fuel fabrication at CEA Marcoule. *J. Nucl. Mater.* 2013, 438, 99−107.

(2) Lebreton, F.; Prieur, D.; Horlait, D.; Delahaye, T.; Jankowiak, A.; Léorier, C.; Jorion, F.; Gavilan, E.; Desmoulière, F. Recent progress on minor actinide bearing oxide fuel fabrication at CEA Marcoule. *J. Nucl. Mater.* 2013, 438, 99−107.

(3) Chollet, M.; Belin, R. C.; Richaud, J. C.; Reynaud, M.; Adenot, F. High temperature X ray diffraction study of uranium−neptunium mixed oxides. *Inorg. Chem.* 2013, 52, 2519−2525.

(4) Yamashita, T.; Nitani, N.; Ohuchi, K.; Muromura, T.; Tsuji, T.; Inagaki, H.; Kato, T. Phase relations of the uranium neptunium oxygen system. *J. Alloys Compd.* 1994, 213/214, 375−377.

(5) Yamashita, T.; Ohuchia, K.; Tsuji, T.; Kato, T.; Ochida, M.; Iwashita, M. *J. Alloys Compd.* 1998, 271−273, 400−403.

(6) Boeuf, A.; Caciuffo, R.; Pagès, M.; Rebizant, J.; Rustichelli, F.; Tabuteau, A. Neutron diffraction study of the $U_{1-x}Np_xO_2$ fluorites. *Europhys. Lett.* 1987, 3, 221.

(7) Tabuteau, A.; Jové, J.; Pagès, M.; de Novion, C. H.; Gal, J. Mössbauer and magnetization studies of the $U_{1-x}Np_xO_2$ fluorites. *Solid State Commun.* 1984, 50, 357−361.

(8) Wilkins, S. B.; Paixão, J. A.; Caciuffo, R.; Javorsky, P.; Wastin, F.; Rebizant, J.; Detlefs, C.; Bernhoeft, N.; Santini, P.; Lander, G. H. *Phys. Rev. B* 2004, 70, 214402.

(9) Tabuteau, A.; Pagés, M.; Bœuf, A.; Rebizant, J.; Manes, L.; Caciuffo, R.; Rustichelli, F. *J. Phys. Lett.* 1984, 45, 373.

(10) Hubert, S.; Purans, J.; Heisbourg, G.; Moisy, P.; Dacheux, N. Local structure of actinide dioxide solid solutions $Th_{1-x}U_xO_2$ and $Th_{1-x}Pu_xO_2$. *Inorg. Chem.* 2006, 45, 3887−3894.

(11) Martin, P.; Grandjean, S.; Valot, C.; Carlot, G.; Ripert, M.; Blanc, P.; Hennig, C. XAS study of $(U_{1-y}Pu_y)O_2$ solid solutions. *J. Alloys Compd.* 2007, 444−445, 410−414.

(12) Cheetham, A. K; Dobson, C. M; Grey, C. P.; Jakeman, R. J. B. Paramagnetic shift probes in high resolution solid state NMR. *Nature* 1987, 328, 706−707.

(13) Grey, C. P.; Smith, M. E.; Cheetham, A. K.; Dobson, C. M.; Dupree, R. Paramagnetic shifts in the ⁸⁹Y MAS NMR of rare earth doped yttrium pyrochlores. *J. Am. Chem. Soc.* 1990, 112, 4670−4675.

(14) Grey, C. P.; Dobson, C. M.; Cheetham, A. K.; Jakeman, R. J.B. Studies of rare earth stannates by ¹¹⁹Sn MAS NMR. The use of paramagnetic shifts probes in the solid state. *J. Am. Chem. Soc.* 1989, 111, 505−511.

(15) Fernández Carrión, A. J.; Allix, M.; Florian, P.; Suchomel, M. R.; Becerro, A. I. Revealing structural detail in the high temperature $La_2Si_2O_7−Y_2Si_2O_7$ phase diagram by synchrotron powder diffraction and nuclear magnetic resonance spectroscopy. *J. Phys. Chem. C* 2012, 116, 21523−21535.

(16) George, N. C.; Pell, A. J.; Dantelle, G.; Page, K.; Llobet, A.; Balasubramanian, M.; Pintacuda, G.; Chmelka, B. F.; Seshadri, R. Local environments of dilute activator ions in the solid state lighting phosphor $Y_{3-x}Ce_xAl_5O_{12}$. *Chem. Mater.* 2013, 25, 3979−3995.

(17) Farnan, I.; Cho, H.; Weber, W. J. Quantification of actinide α radiation damage in minerals and ceramics. *Nature* 2007, 445, 190−193.

(18) Martel, L.; Magnani, N.; Vigier, J. F.; Boshoven, J.; Selfslag, C.; Farnan, I.; Griveau, J. C.; Somers, J.; Fanghänel, T. High resolution solid state oxygen 17 NMR of actinide bearing compounds: an insight into the 5f chemistry. *Inorg. Chem.* 2014, 53, 6928−6933.

(19) Yamashita, T.; Nitani, N.; Tsuji, T. Thermal expansion of neptunium uranium mixed oxides. *J. Nucl. Mater.* 1997, 247, 90−93.

(20) Sood, D. D. The role sol−gel process for nuclear fuels an overview. *J. Sol Gel Sci. Technol.* 2011, 59, 404−416.

(21) Petricek, V.; Dusek, M.; Palatinus, L. *Jana 2006: The Crystallographic Computing System*; Institute of Physics: Czech Republic, 2006

(22) Rothe, J.; Butorin, S.; Dardenne, K.; Denecke, M. A.; Kienzler, B.; Löble, M.; Metz, V.; Seibert, A.; Steppert, M.; Vitova, T.; Walther, C.; Geckeis, H. The INE Beamline for actinide science at ANKA. *Rev. Sci. Instrum.* 2012, 83, 043105−13.

(23) Martel, L.; Somers, J.; Berkmann, C.; Koepp, F.; Rothermel, A.; Pauvert, O.; Selfslag, C.; Farnan, I. A nuclear magnetic resonance spectrometer concept for hermetically sealed magic angle spinning investigations on highly toxic, radiotoxic, or air sensitive materials. *Rev. Sci. Instrum.* **2013**, *84*, 055112.

(24) Massiot, D.; Fayon, F.; Capron, M.; King, I.; Le Calvé, S.; Alonso, B.; Durand, J. O.; Bujoli, B.; Gan, Z.; Hoatson, G. Modelling one and two dimensional solid state NMR spectra. *Magn. Reson. Chem.* **2002**, *40*, 70−76.

(25) Williamson, G. K.; Hall, W. H. X ray line broadening from filed aluminium and wolfram. *Acta Metall.* **1953**, *1*, 22−31.

(26) Venkateswara Rao, K.; Sunandana, C. S. XRD, microstructural and EPR susceptibility characterization of combustion synthesized nanoscale $Mg_{1-x}Ni_xO$ solid solutions. *J. Phys. Chem. Solids* **2008**, *69*, 87−96.

(27) Düvel, A.; Ruprecht, B.; Heitjans, P.; Wilkening, M. Mixed alkaline earth effect in the metastable anion conductor $Ba_{1-x}Ca_xF_2$ (0 ≤ x ≤1): Correlating long range ion transport with local structures revealed by ultrafast ^{19}F MAS NMR. *J. Phys. Chem. C* **2011**, *115*, 23784−23789.

(28) Allix, M.; Alba, M. D.; Florian, P.; Fernandez Carrion, A. J.; Suchomel, M. R.; Escudero, A.; Suard, E.; Becerro, A. I. Structural elucidation of β $(Y,Sc)_2Si_2O_7$: combined use of ^{89}Y MAS NMR and powder diffraction. *J. Appl. Crystallogr.* **2011**, *44*, 846−852.

(29) Fernandez Carrion, A. J.; Escudero, A.; Suchomel, M. R.; Becerro, A. I. Structural and kinetic study of phase transitions in $LaYSi_2O_7$. *J. Eur. Ceram. Soc.* **2012**, *32*, 2477−2486.

(30) Escudero, A.; Alba, M. D.; Becerro, A. I. Polymorphism in the $Sc_2Si_2O_7-Y_2Si_2O_7$ system. *J. Solid State Chem.* **2007**, *180*, 1436−1445.

(31) Düvel, A.; Wegner, S.; Efimov, K.; Feldhoff, A.; Heitjans, P.; Wilkening, M. Access to metastable complex ion conductors viamechanosynthesis: preparation, microstructure and conductivity of $(Ba,Sr)LiF_3$ with inverse perovskite structure. *J. Mater. Chem.* **2011**, *21*, 6238−6250.

(32) Youngman, R. E.; Smith, C. M. Multinuclear NMR studies of mixed crystals. *Phys. Rev. B* **2008**, *78*, 014112.

(33) Kentgens, A. P. M. A practical guide to solid state NMR of half integer quadrupolar nuclei with some applications to disordered systems. *Geoderma* **1997**, *80*, 271−306.

(34) Freude, D.; Haase, J. Quadrupole effects in solid state nuclear magnetic resonance. *NMR Basic Principles Prog.* **1993**, *29*, 1−90.

(35) Smith, M. E.; van Eck, E. R. H. Recent advances in experimental solid state NMR methodology for half integer spin quadrupolar nuclei. *Prog. Nucl. Magn. Reson. Spectrosc.* **1999**, *34*, 159−201.

(36) Freude, D. Quadrupolar Nuclei in Solid state Nuclear Magnetic Resonance. *Encyclopedia of Analytical Chemistry*; John Wiley and Sons Ltd: New York, 2006.

(37) Fenzke, D.; Freude, D.; Fröhlich, T.; Haase, J. NMR intensity measurements of half integer quadrupole nuclei. *Chem. Phys. Lett.* **1984**, *111*, 171−175.

(38) Man, P. P. Investigation of the central line of ^{55}Mn in $KMnO_4$ by a two dimensional NMR method. *J. Magn. Reson.* **1986**, *67*, 78−90.

(39) Nielsen, N. C.; Bildsoe, H.; Jakobsen, H. J. Finite rf pulse excitation in MAS NMR of quadrupolar nuclei. Quantitative aspects and multiple quantum excitation. *Chem. Phys. Lett.* **1992**, *191*, 205.

(40) Nielsen, N. C.; Bildsoe, H.; Jakobsen, H. J. Multiple quantum MAS nutation NMR spectroscopy of quadrupolar nuclei. *J. Magn. Reson.* **1992**, *97*, 149.

(41) Massiot, D.; Bessada, C.; Coutures, J. P.; Taulelle, F. A quantitative study of ^{27}Al MAS NMR in crystalline YAG. *J. Magn. Reson.* **1990**, *90*, 231−242.

Repository KITopen

Dies ist ein Postprint/begutachtetes Manuskript.